

TumorGen: Boundary-Aware Tumor-Mask Synthesis with Rectified Flow Matching

Shengyuan Liu^{1*}, Wenting Chen^{2*}, Boyun Zheng¹, Wentao Pan¹,
Xiang Li^{3†}, and Yixuan Yuan^{1†}

¹ The Chinese University of Hong Kong

² City University of Hong Kong

³ Massachusetts General Hospital and Harvard Medical School

Abstract. Tumor data synthesis offers a promising solution to the shortage of annotated medical datasets. However, current approaches either limit tumor diversity by using predefined masks or employ computationally expensive two-stage processes with multiple denoising steps, causing computational inefficiency. Additionally, these methods typically rely on binary masks that fail to capture the gradual transitions characteristic of tumor boundaries. We present TumorGen, a novel Boundary-Aware Tumor-Mask Synthesis with Rectified Flow Matching for efficient 3D tumor synthesis with three key components: a Boundary-Aware Pseudo Mask Generation module that replaces strict binary masks with flexible bounding boxes; a Spatial-Constraint Vector Field Estimator that simultaneously synthesizes tumor latents and masks using rectified flow matching to ensure computational efficiency; and a VAE-guided mask refiner that enhances boundary realism. TumorGen significantly improves computational efficiency by requiring fewer sampling steps while maintaining pathological accuracy through coarse and fine-grained spatial constraints. Experimental results demonstrate TumorGen’s superior performance over existing tumor synthesis methods in both efficiency and realism, offering a valuable contribution to AI-driven cancer diagnostics.

Keywords: Tumor Synthesis · Flow-Based Model · Generative Model

1 Introduction

AI-driven tumor diagnostic systems [3,24,26] are revolutionizing early cancer screening and detection, offering unprecedented precision, efficiency, and accessibility in identifying malignancies at their most treatable stages. While these computational approaches show promising results, their performance heavily relies on large-scale, high-quality annotated tumor data for training [19,25]. However, obtaining such annotations requires extensive manual effort from medical professionals, making it both time-consuming and cost-prohibitive [13,29]. A

* Equal contributions.

† Corresponding author: Xiang Li (xli60@mgh.harvard.edu), Yixuan Yuan (yxyuan@ee.cuhk.edu.hk)

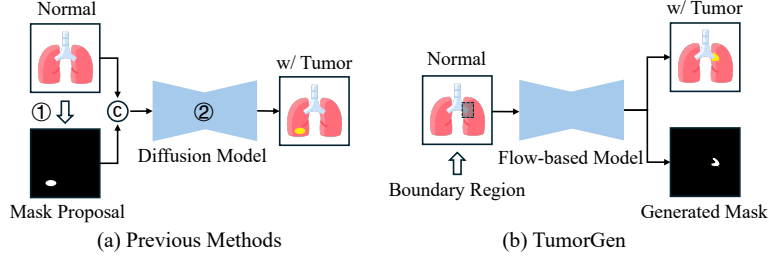


Fig. 1: (a) Previous two-stage tumor synthesis methods need to specify the pixel-wise mask. (b) TumorGen can synthesize both the tumor image and the corresponding mask with only a rough bounding box.

potential solution is to synthesize tumor data, offering a scalable approach to expand training datasets without the burden of manual annotation.

Current tumor synthesis methods [4,8,12,15,20,28,30] can be broadly categorized into two groups. The first group utilizes the pre-defined tumor masks as direct input for synthesis [4,8,12,20,28], which may limit the diversity of the tumor shape. The second group employs a two-stage approach, where a tumor mask is initially generated followed by tumor synthesis [15,30], as shown in Fig. 1 (a). These methods first generate tumor masks by identifying potential tumor locations and creating shapes based on these proposals, then generate tumors according to these masks. The first challenge is that while this two-stage strategy enables more diverse tumor morphologies, its sequential nature introduces significant computational overhead. Additionally, these methods commonly employ diffusion models [10,21] for tumor generation, which require multiple denoising steps (50 to 1,000 steps) during the inference process. Thus, there is a pressing need for more efficient tumor synthesis approaches.

Another challenge is that current methods leverage binary masks for tumor synthesis, ignoring the characteristics of tumor boundaries. These masks can be generated either through rule-based approaches [4,8,12,28] or data-driven methods [15,30]. Rule-based methods typically generate masks using morphological operations on ellipsoidal primitives, which may not accurately represent the diverse shapes and sizes of real tumors. While data-driven approaches learn to generate masks from real tumor data, they often produce strict boundaries that fail to capture the inherent characteristics of tumor regions. Unlike natural images with clear object boundaries, medical pathologies such as tumors exhibit soft, gradual transitions between diseased and healthy tissues [16,17]. The binary nature of current mask generation methods overlooks these soft boundaries, potentially compromising the fidelity of synthesized tumors. Therefore, incorporating boundary characteristics into tumor mask generation is crucial for improving the quality of tumor synthesis.

To address these challenges, we introduce a Rectified Flow-based Boundary-Aware Tumor-Mask Synthesis framework, named **TumorGen**. Our framework

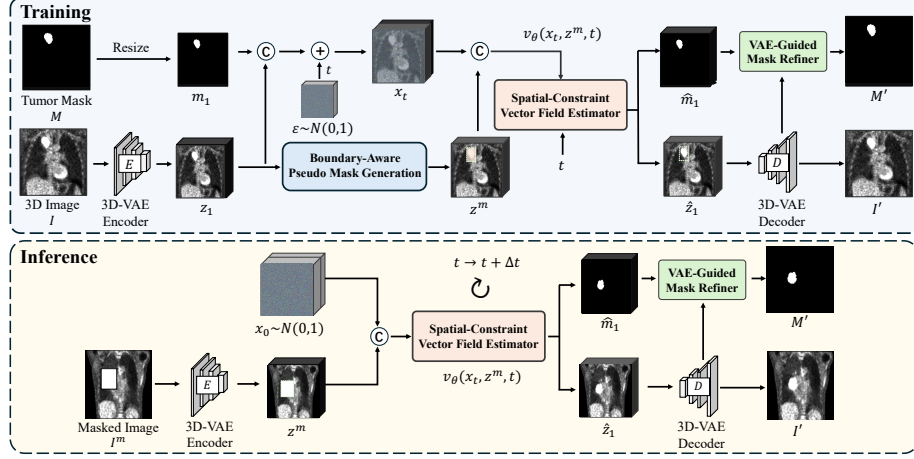


Fig. 2: Overview of **TumorGen**, a rectified flow-based 3D tumor synthesis framework with a Boundary-Aware Pseudo Mask Generation module (BA-PMG) to automatic tumor bounding box generation, a Spatial-Constraint Vector Field Estimator (SC-VFE) for simultaneous tumor image and mask synthesis, and a VAE-guided mask refiner (VMR) to enhance mask boundary.

consists of three key components: a *Boundary-Aware Pseudo Mask Generation module (BA-PMG)*, a *Spatial-Constraint Vector Field Estimator (SC-VFE)*, and a *VAE-guided mask refiner (VMR)*. The framework efficiently synthesizes 3D tumors using only a bounding box to indicate potential tumor regions. To consider the **characteristics of tumor boundary**, the BA-PMG module automatically generates a bounding box for potential tumor regions, replacing the conventional strict binary mask approach and allowing for more flexible tumor generation. In order to enhance **computational efficiency**, our SC-VFE module simultaneously synthesizes both tumor image latents and their corresponding masks using rectified flow matching, which requires fewer sampling steps by establishing straight mapping between noise and data. Aiming to enhance the realism of generated tumors, the SC-VFE implements two crucial spatial constraints. At a coarse level, we compare ground-truth (GT) and synthetic tumors within the bounding box to ensure overall consistency. For fine-grained control, we leverage the generated tumor mask to align GT and synthetic tumors specifically within the tumor region, ensuring detailed pathological accuracy. To achieve precise and realistic tumor boundaries, our VMR module refines the generated tumor mask using hierarchical features from the 3D-VAE decoder. Finally, 3D-VAE decodes synthetic tumor image latents into the final tumor image. Extensive experimental results demonstrate both the effectiveness of each component and the overall superiority of TumorGen compared to existing tumor synthesis methods.

2 TumorGen

Overview. As shown in Fig. 2, given a 3D image $I \in \mathbb{R}^{H \times W \times D}$ and corresponding tumor mask $M \in \{0, 1\}^{H \times W \times D}$, we first compress the image using a 3D variational autoencoder (3D-VAE) E to encode the image from the pixel-space into the latent space $z_1 = E(I) \in \mathbb{R}^{\frac{H}{4} \times \frac{W}{4} \times \frac{D}{4} \times 4}$, and downsample the tumor mask M to match the dimensions of z_1 , obtaining resized tumor mask m_1 . Subsequently, we employ the Boundary-Aware Pseudo Mask Generation module (BA-PMG) to generate a potential bounding box (bbox) B for the image latents z_1 , and create a masked image feature z^m by removing the bbox region from z_1 . We then concatenate z_1 and m_1 and incorporate initial noise from a normal distribution $\mathcal{N}(0, 1)$ into the concatenation using time step t as weight, yielding $x_t = (1 - t)\epsilon + t \cdot x_1$. The Spatial-Constraint Vector Field Estimator (SC-VFE) processes the concatenation of x_t and z^m to simultaneously predict the tumor image latents \hat{z}_1 and its mask image \hat{m}_1 . Then, the 3D-VAE decodes \hat{z}_1 into a high-quality 3D image I' . To enhance tumor boundary precision, the VAE-guided Mask Refiner (VMR) processes the predicted mask image \hat{m}_1 while incorporating embeddings from the 3D-VAE of \hat{z}_1 to generate the refined mask image M' . Finally, 3D-VAE decodes the tumor image latents \hat{z}_1 to the final tumor image I' .

2.1 Boundary-Aware Pseudo Mask Generation (BA-PMG)

Previous tumor synthesis methods rely on binary masks, failing to capture the gradual transitions between tumor and healthy tissue and causing unrealistic synthetic tumors. Thus, we propose a boundary-aware pseudo mask generation (BA-PMG) approach that automatically generates adaptive bounding boxes around potential tumor regions, enabling more natural tumor synthesis.

Specifically, given a resized tumor mask m_1 , we first compute a tight bounding box B' encompassing the tumor by identifying the minimum and maximum coordinates of tumor voxels in each dimension. To determine the final bounding box B , we define offset distances $d = (d_x, d'_x), (d_y, d'_y), (d_z, d'_z)$ between the planes of B and B' , where the pairs represent offsets along the x , y , and z axes respectively. These offsets are randomly sampled from a uniform distribution within a range proportional to the image dimensions (width W , height H , and depth D) of the 3D image I . Specifically, each offset is sampled as $d_i \sim U(0, \alpha D_i)$, where D_i is the respective dimension and α is a scaling factor controlling the maximum extension. The final bounding box B is obtained by expanding B' by these offsets: $B = B' + d$. This adaptive expansion allows the model to consider varying amounts of surrounding tissue context. We then mask the image latents z_1 using B to obtain masked latents $z^m = (1 - B) \odot z_1$, where \odot denotes element-wise multiplication. The masked latents retain information about both the tumor region and its surrounding context, which is crucial for learning realistic boundary transitions. The BA-PMG module enables the synthesis model to learn realistic tumor boundary characteristics during generation, moving beyond the limitations of strict binary foreground annotations.

2.2 Spatial-Constraint Vector Field Estimator (SC-VFE)

Although two-stage tumor synthesis models can generate diverse tumor morphologies, they suffer from computational inefficiency due to their separate mask generation step. Thus, we introduce a Spatial-Constraint Vector Field Estimator (SC-VFE) that leverages Rectified Flow Matching (RFM) [5,6] to simultaneously generate tumor images and their corresponding masks by establishing straight paths between noise and data. To enhance synthetic tumor realism, we implement both coarse-grained and fine-grained spatial constraints, ensuring overall anatomical consistency while preserving detailed pathological features.

Formally, we define the latent space of tumor image z and its mask image m as a joint variable $x = [z, m]$. We employ RFM to learn a vector field estimator v_θ that models a reversible mapping from an initial normal distribution $\mathcal{N}(0, 1)$ to the target joint distribution $x \sim p_1(z, m)$ along straight paths. Then, we concatenate tumor image latents z_1 (encoded by a 3D VAE encoder) with resized mask image m_1 . For the forward process over time t , we perform element-wise addition between the concatenation output and initial noise sampled from a normal distribution $\mathcal{N}(0, 1)$, yielding $x_t = (1 - t)\epsilon + t \cdot x_1$, where $x_1 = [z_1, m_1]$ is the concatenation of the tumor image latents z_1 and its corresponding mask m_1 , and $\epsilon \sim \mathcal{N}(0, 1)$ denotes sampled random noise. With x_t and masked image latents z^m , vector field estimator v_θ outputs the estimated vector field v_θ^z, v_θ^m for synthetic tumor image latents \hat{z}_1 and mask images \hat{m}_1 , $v_\theta(x_t, z^m, t) = [v_\theta^z, v_\theta^m]$. Subsequently, the synthetic tumor image latents \hat{z}_1 and its mask image \hat{m}_1 are computed by:

$$\hat{z}_1 = z_t + (1 - t) \cdot v_\theta^z, \quad \hat{m}_1 = m_t + (1 - t) \cdot v_\theta^m, \quad (1)$$

$$z_t = (1 - t)\epsilon + t \cdot z_1, \quad m_t = (1 - t)\epsilon + t \cdot m_1, \quad (2)$$

To optimize the vector field estimator, we utilize the RFM [6] objective function, which is defined as:

$$\mathcal{L}_{rfm}(\theta) = \mathbb{E}_{t, \epsilon \sim \mathcal{N}(0, 1), x \sim p_1(z, m)} \|v_\theta(x_t, z^m, t) - (x_1 - \epsilon)\|^2 \quad (3)$$

To improve the realism of synthetic tumors, we impose a coarse-grained spatial constraint and a fine-grained spatial constraint on the synthetic tumor image latents, respectively. To preserve the overall consistency, we propose a coarse-grained spatial constraint \mathcal{L}_{coarse} , which utilizes the final bounding box generated by BA-PMG module to minimize the difference between the ground-truth (GT) image latents z_1 and the synthetic tumor image latents \hat{z}_1 inside the bounding box,

$$\mathcal{L}_{coarse}(\theta) = \mathbb{E}_{t, \epsilon \sim \mathcal{N}(0, 1), x \sim p_1(z, m)} \|B \odot \hat{z}_1 - B \odot z_1\|^2. \quad (4)$$

To preserve the detailed pathological accuracy, we design a fine-grained spatial constraint \mathcal{L}_{fine} to leverage the generated tumor mask to narrow the Structural Similarity (SSIM) distance between GT image latents z_1 and synthetic tumor image latents \hat{z}_1 inside the tumor mask,

$$\mathcal{L}_{fine}(\theta) = \mathbb{E}_{t, \epsilon \sim \mathcal{N}(0, 1), x \sim p_1(z, m)} [1 - SSIM(\hat{m}_1 \odot \hat{z}_1, m_1 \odot z_1)]. \quad (5)$$

By adopting the SC-VFE module, we can enable the simultaneous synthesis of tumor and mask images and preserve the realism of the synthetic tumor at both coarse and fine grained levels, thereby eliminating the need for manually specifying pixel-wise tumor mask.

2.3 VAE-Guided Mask Refiner (VMR)

Since flow matching occurs in latent space, the generated tumor masks have poor resolution and cannot properly align with the VAE decoder’s output images. To generate precise tumor mask images, we propose a VAE-Guided Mask Refiner (VMR) that leverages the spatial information from the VAE model to refine tumor mask boundaries.

Specifically, a 3D VAE decoder transforms synthetic tumor image latents \hat{z}_1 into a tumor image I' and extracts corresponding features $f = \{f_1, f_2, f_3\}$ from three different decoder layers. These hierarchical features f are processed through convolutional layers to obtain $f' = \{f'_1, f'_2, f'_3\}$. The VMR module f_θ then takes the generated tumor mask \hat{m}_1 as input and performs element-wise addition between its layer features $q = \{q_1, q_2, q_3\}$ and the corresponding features in $f' = \{f'_1, f'_2, f'_3\}$ to produce the refined tumor mask M' . To optimize the refined tumor mask, we compute the reconstruction loss between the ground truth and refined mask image:

$$\mathcal{L}_{rec}(\theta) = \mathbb{E}_{t, \epsilon \sim \mathcal{N}(0,1), x \sim p_1(z, m)} \|f_\theta(\hat{m}_1) - M\|^2, \quad (6)$$

where $f_\theta(\hat{m}_1)$ represents the refined tumor mask M' , and M is the ground truth tumor mask. This loss function ensures high-resolution mask generation that closely aligns with the image content by minimizing the difference between the generated and ground truth masks.

Finally, the overall objective function for the proposed method integrates four components: the rectified flow matching objective function, coarse-grained spatial constraint, fine-grained spatial constraint, and reconstruction loss for the refined mask image. These components are combined as:

$$\mathcal{L} = \mathcal{L}_{rfm} + \lambda_1 \mathcal{L}_{coarse} + \lambda_2 \mathcal{L}_{fine} + \lambda_3 \mathcal{L}_{rec}, \quad (7)$$

where λ_1 , λ_2 , and λ_3 are weighting coefficients.

3 Experiments

3.1 Experimental Setting

Datasets. The experiments use two public available Positron Emission Tomography (PET) datasets: Hecktor-2021 [1] with 224 PET scans (200 training, 24 testing) and AutoPET [7] with 168 whole-body PET scans from lung cancer patients (153 training, 15 testing). For AutoPET, TotalSegmentator [27] is used

Table 1: Quantitative evaluation on the Hecktor and AutoPET datasets. A, S, C denotes Axial, Sagittal, and Coronal planes. Avg denotes the average result.

Method	Hecktor				AutoPET			
	FID(A)	FID(S)	FID(C)	FID(Avg)	FID(A)	FID(S)	FID(C)	FID(Avg)
HA-GAN [22]	137.561	103.794	114.298	118.551	130.187	152.133	128.709	137.010
MedFusion [23]	144.625	125.834	87.517	119.325	138.462	129.524	136.280	134.755
BLD [2]	75.718	56.883	73.486	68.696	72.371	114.110	109.307	98.596
SynTumor [12]	93.024	85.035	91.042	89.701	108.671	98.704	119.638	109.004
DiffTumor [4]	80.281	52.659	67.523	66.821	82.394	96.248	76.195	84.946
TumorGen	54.877	39.633	61.593	52.035	66.432	66.933	83.934	72.433

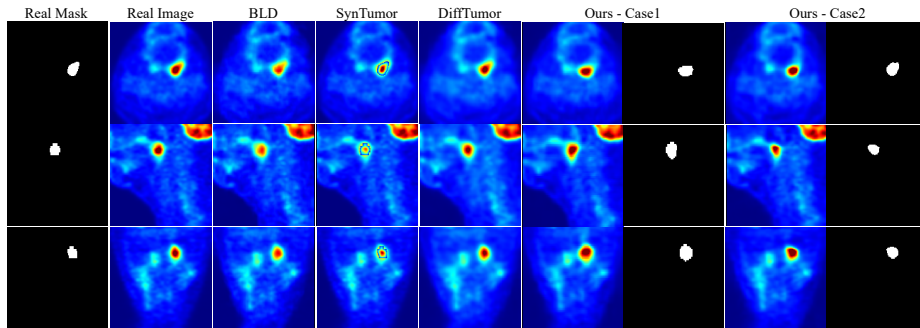


Fig. 3: Qualitative comparison among different synthesis methods.

to segment lung regions, which were then cropped to $200 \times 200 \times 100$ and resized to $128 \times 128 \times 64$ for training. All scans include both PET images and corresponding tumor segmentation masks.

Implementation details and metrics. We use a pre-trained 3D KL-VAE [8] as 3D-VAE. For spatial-constraint vector field estimation, we implement a 3D U-Net architecture. For evaluation, image quality is evaluated using Fréchet Inception Distance (FID) [9]. We calculate the FID on the middle slices on axial, coronal, and sagittal planes of the generated 3D images following [11]. Moreover, to evaluate the alignment quality of synthesized image-mask pairs by TumorGen, we use a pre-trained nnU-Net [14] on the synthesized images to obtain predicted masks, and calculate both Dice Similarity Coefficient (DSC) and Normalized Surface Distance (NSD) with the generated masks.

3.2 Experimental Results

Comparison with Previous Methods. We compare our TumorGen with existing tumor synthesis methods, including the conditional generation methods (HA-GAN [22] and MedFusion [18]), and the two-stage methods that generate tumors by pre-defined masks (SynTumor [12], BLD [2], and DiffTumor [4]). In

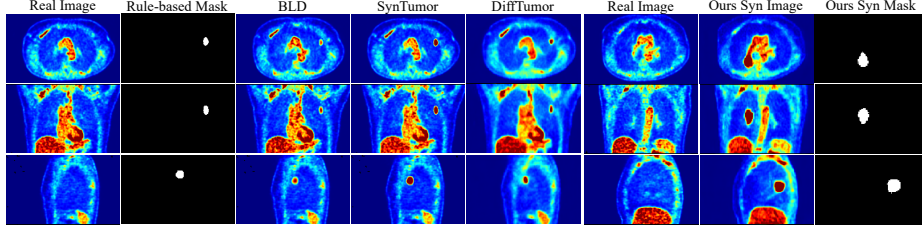


Fig. 4: Tumor images generated from healthy images.

Table 2: Ablation study on Hecktor dataset.

BA-PMG	SC-VFE		VMR	Metrics		
	Coarse	Fine		FID	DSC	NSD
✗	✓	✓	✓	66.263	0.677	0.711
✓	✗	✓	✓	55.416	0.660	0.673
✓	✓	✗	✓	63.611	0.680	0.713
✓	✓	✓	✗	54.279	0.614	0.577
✓	✓	✓	✓	52.035	0.694	0.741

Table 3: Comparison of inference time.

Methods	Sampling	FID	Inference Time (s)
DiffTumor	DDPM-50	66.821	1.226
DiffTumor	DDIM-50	68.306	1.133
TumorGen	RFM-50	52.035	1.061
TumorGen	RFM-10	55.862	0.218

Table 1, our TumorGen surpasses the DiffTumor [4] by 14 in average FID on the Hecktor dataset, implying our superiority to existing methods. For qualitative evaluation, Fig. 3 shows that TumorGen can synthesize realistic tumors with better tumor boundaries and also provide great diversity of the tumor shape.

Ablation Study. To prove the effectiveness of each module in TumorGen, we conduct the ablation study on the Hecktor dataset [1]. We evaluate the synthetic tumor image quality using FID score, and Table 2 shows that ablating each component leads to performance decreases, suggesting the effectiveness of each component. Moreover, we evaluate the alignment of generated image-mask pairs using DSC and NSD metrics. The results demonstrate that our generated tumor masks maintain high consistency with the corresponding images, and the introduction of VMR significantly enhances this alignment.

Efficiency Analysis. We compute the inference time (seconds) for DiffTumor [4] with 50-step DDPM [10] and DDIM [21] samplers, and compare with our method using both 10 and 50 sampling steps with RFM. Table 3 shows that our method generates each sample in 0.218s using a 10-step RFM, while achieving an FID of 55.862, highlighting the computational efficiency of TumorGen.

Generalizability to Healthy Subjects. We evaluate the generalization capability of TumorGen in the healthy subjects. As shown in Fig. 4, TumorGen can synthesize the realistic tumors in the lung region across three planes, suggesting its strong capability in generalizing in PET imaging of healthy patients.

4 Conclusions

TumorGen addresses key limitations in tumor synthesis through three innovative components: BA-PMG, SC-VFE, and VMR. Our experiments on two PET datasets show superior performance over existing methods with significantly improved FID scores and strong segmentation metrics. TumorGen achieves greater computational efficiency while maintaining high-quality outputs and demonstrates effective generalization to healthy subjects.

References

1. Andrearczyk, V., Oreiller, V., Boughdad, S., Rest, C.C.L., Elhalawani, H., Jreige, M., Prior, J.O., Vallières, M., Visvikis, D., Hatt, M., et al.: Overview of the hecktor challenge at miccai 2021: automatic head and neck tumor segmentation and outcome prediction in pet/ct images. In: 3D head and neck tumor segmentation in PET/CT challenge, pp. 1–37. Springer (2021)
2. Avrahami, O., Fried, O., Lischinski, D.: Blended latent diffusion. *ACM Trans. Graph.* **42**(4), 1–11 (2023)
3. Cao, K., Xia, Y., Yao, J., Han, X., Lambert, L., Zhang, T., Tang, W., Jin, G., Jiang, H., Fang, X., et al.: Large-scale pancreatic cancer detection via non-contrast ct and deep learning. *Nat. Med.* **29**(12), 3033–3043 (2023)
4. Chen, Q., Chen, X., Song, H., Xiong, Z., Yuille, A., Wei, C., Zhou, Z.: Towards generalizable tumor synthesis. In: CVPR. pp. 11147–11158 (2024)
5. Chen, R.T., Rubanova, Y., Bettencourt, J., Duvenaud, D.K.: Neural ordinary differential equations. *NeurIPS* **31** (2018)
6. Esser, P., Kulal, S., Blattmann, A., Entezari, R., Müller, J., Saini, H., Levi, Y., Lorenz, D., Sauer, A., Boesel, F., et al.: Scaling rectified flow transformers for high-resolution image synthesis. In: ICML (2024)
7. Gatidis, S., Hepp, T., Früh, M., La Fougère, C., Nikolaou, K., Pfannenberger, C., Schölkopf, B., Küstner, T., Cyran, C., Rubin, D.: A whole-body fdg-pet/ct dataset with manually annotated tumor lesions. *Sci. Data* **9**(1), 601 (2022)
8. Guo, P., Zhao, C., Yang, D., Xu, Z., Nath, V., Tang, Y., Simon, B., Belue, M., Harmon, S.A., Turkbey, B., et al.: Maisi: Medical ai for synthetic imaging. *CoRR* (2024)
9. Heusel, M., Ramsauer, H., Unterthiner, T., Nessler, B., Hochreiter, S.: Gans trained by a two time-scale update rule converge to a local nash equilibrium. *NeurIPS* **30** (2017)
10. Ho, J., Jain, A., Abbeel, P.: Denoising diffusion probabilistic models. *NeurIPS* **33**, 6840–6851 (2020)
11. Hong, S., Marinescu, R., Dalca, A.V., Bonkhoff, A.K., Bretzner, M., Rost, N.S., Golland, P.: 3d-stylegan: A style-based generative adversarial network for generative modeling of three-dimensional medical images. In: MICCAI Workshop. pp. 24–34. Springer (2021)
12. Hu, Q., Chen, Y., Xiao, J., Sun, S., Chen, J., Yuille, A.L., Zhou, Z.: Label-free liver tumor segmentation. In: CVPR. pp. 7422–7432 (2023)
13. Ibrahim, H., Liu, X., Zariffa, N., Morris, A.D., Denniston, A.K.: Health data poverty: an assailable barrier to equitable digital health care. *Lancet Digital Health* **3**(4), e260–e265 (2021)

14. Isensee, F., Jaeger, P.F., Kohl, S.A., Petersen, J., Maier-Hein, K.H.: nnu-net: a self-configuring method for deep learning-based biomedical image segmentation. *Nat. Methods* **18**(2), 203–211 (2021)
15. Kim, K., Cho, H., Na, Y., Ye, S.J., Lee, J., Ahn, S.S., Park, J.E., Kim, H.: A tumor inpainting framework for mri using automated masks based on channel-specific conditions across the volume. *Biomed. Signal Process. Control* **105**, 107579 (2025)
16. Lei, M., Wu, H., Lv, X., Wang, X.: Condseg: A general medical image segmentation framework via contrast-driven feature enhancement. *AAAI* (2025)
17. Liu, S., Chen, Z., Yang, Q., Yu, W., Dong, D., Hu, J., Yuan, Y.: Polyp-gen: Realistic and diverse polyp image generation for endoscopic dataset expansion. *ICRA* (2025)
18. Müller-Franzes, G., Niehues, J.M., Khader, F., Arasteh, S.T., Haarbuerger, C., Kuhl, C., Wang, T., Han, T., Nolte, T., Nebelung, S., et al.: A multimodal comparison of latent denoising diffusion probabilistic models and generative adversarial networks for medical image synthesis. *Sci. Rep.* **13**(1), 12098 (2023)
19. Pan, X., AbdulJabbar, K., Coelho-Lima, J., Grapa, A.I., Zhang, H., Cheung, A.H.K., Baena, J., Karasaki, T., Wilson, C.R., Sereno, M., et al.: The artificial intelligence-based model anorak improves histopathological grading of lung adenocarcinoma. *Nat. Cancer* **5**(2), 347–363 (2024)
20. Peng, L., Zhang, Z., Durak, G., Miller, F.H., Medetalibeyoglu, A., Wallace, M.B., Bagci, U.: Optimizing synthetic data for enhanced pancreatic tumor segmentation. In: *PILM Workshop*. pp. 35–44. Springer (2024)
21. Song, J., Meng, C., Ermon, S.: Denoising diffusion implicit models. In: *ICLR* (2020)
22. Sun, L., Chen, J., Xu, Y., Gong, M., Yu, K., Batmanghelich, K.: Hierarchical amortized gan for 3d high resolution medical image synthesis. *IEEE J. Biomed. Health Inform.* **26**(8), 3966–3975 (2022)
23. Thambawita, V., Salehi, P., Sheshkal, S.A., Hicks, S.A., Hammer, H.L., Parasa, S., Lange, T.d., Halvorsen, P., Riegler, M.A.: Singan-seg: Synthetic training data generation for medical image segmentation. *PloS one* **17**(5), e0267976 (2022)
24. Wang, J., Wang, K., Yu, Y., Lu, Y., Xiao, W., Sun, Z., Liu, F., Zou, Z., Gao, Y., Yang, L., et al.: Self-improving generative foundation model for synthetic medical image generation and clinical applications. *Nat. Med.* pp. 1–9 (2024)
25. Wang, J., Yu, Y., Tan, Y., Wan, H., Zheng, N., He, Z., Mao, L., Ren, W., Chen, K., Lin, Z., et al.: Artificial intelligence enables precision diagnosis of cervical cytology grades and cervical cancer. *Nat. Commun.* **15**(1), 4369 (2024)
26. Wang, X., Zhao, J., Marostica, E., Yuan, W., Jin, J., Zhang, J., Li, R., Tang, H., Wang, K., Li, Y., et al.: A pathology foundation model for cancer diagnosis and prognosis prediction. *Nature* **634**(8035), 970–978 (2024)
27. Wasserthal, J., Breit, H.C., Meyer, M.T., Pradella, M., Hinck, D., Sauter, A.W., Heye, T., Boll, D.T., Cyriac, J., Yang, S., et al.: Totalsegmentator: robust segmentation of 104 anatomic structures in ct images. *Radiol. Artif. Intell.* **5**(5) (2023)
28. Wu, L., Zhuang, J., Ni, X., Chen, H.: Freetumor: Advance tumor segmentation via large-scale tumor synthesis. *ECCV* (2024)
29. Yang, Y., Zhang, H., Gichoya, J.W., Katabi, D., Ghassemi, M.: The limits of fair medical imaging ai in real-world generalization. *Nat. Med.* **30**(10), 2838–2848 (2024)
30. Zhang, Z., Deng, H., Li, X.: Unsupervised liver tumor segmentation with pseudo anomaly synthesis. In: *International Workshop on Simulation and Synthesis in Medical Imaging*. pp. 86–96. Springer (2023)